EES Catalysis

PAPER

View Article Online
View Journal

Check for updates

Cite this: DOI: 10.1039/d5ey00367a

Anodic activation-mediated formation of a crystalline–amorphous heterojunction of CoNi(O)OH for improved urea oxidation activity

Toufik Ansari,[a] Manshu Dhillon,[b] Vijay Patel,[a] Aviru Kumar Basu [b] and Arindam Indra *[a]

Received 31st December 2025,
Accepted 15th March 2026

DOI: 10.1039/d5ey00367a

rsc.li/eescatalysis

The urea oxidation reaction (UOR) has been proposed as an alternative to anodic oxygen evolution for an improved cell voltage and cost-effective H_2 production by water electrolysis. However, the progress in this field is limited by the lack of efficient UOR electrocatalysts. Herein, we report two different active catalysts, [CoNi(O)OHs], formed by the *in situ* anodic activation of the cyanide-bridged polymer [CoNi(O)OH-1] and CoNi-layered double hydroxide [CoNi(O)OH-2] for the electrochemical UOR. In CoNi(O)OH-1, the Co-leaching during the anodic activation produced a Ni-rich CoNi(O)OH phase, forming a crystalline–amorphous heterojunction with a highly disordered structure. The defect-rich structure of CoNi(O)OH-1 facilitates the oxidation of Ni^{2+} to Ni^{3+}, stabilizes the Ni^{3+} valence state, and thereby provides dynamically accessible active sites for the UOR. As a result, CoNi(O)OH-1 achieved a current density of 400 mA cm^{-2} at a potential of 1.34 V *vs.* RHE, far better than that of CoNi(O)OH-2 (1.45 V *vs.* RHE) and Ni(O)OH (1.57 V *vs.* RHE). Furthermore, *operando* Raman spectroscopy reveals the adsorption of urea molecules on the catalyst surface, followed by dehydrogenation, and C–N bond cleavage during the UOR.

Broader context

The urea oxidation reaction (UOR) at the anode has been proposed as an alternative to the oxygen evolution reaction (OER) for an improved cell voltage and cost-effective hydrogen production through water electrolysis. However, progress in this field is limited by the lack of efficient UOR catalysts and an understanding of the underlying mechanisms. Early studies on the UOR primarily reported crystalline Ni-based oxides, layered double hydroxides, and Prussian blue analogs. However, these materials exhibited moderate UOR activity. In this study, we report an active catalyst CoNi(O)OH, formed by the *in situ* anodic activation of a cyanide-bridged polymer. The active catalyst, composed of a heterojunction of amorphous and crystalline phases of Ni(O)OH, improves the charge transfer, facilitates the oxidation of Ni^{2+} to Ni^{3+}, and optimizes the electronic structure to stabilize the Ni^{3+} species, active sites for the UOR. As a result, a tremendous improvement in the UOR activity was observed.

Introduction

The production of green H_2 by electrocatalytic water splitting is largely hindered by the slow reaction kinetics of the anodic oxygen evolution reaction (OER), resulting in a large working voltage (1.5–2.0 V) for electrolysis.[1,2] The substitution of the anodic OER with other thermodynamically favorable oxidation reactions (alcohol oxidation, amine oxidation, and small molecule oxidation) has been successfully explored to reduce the energy requirement of the cell, making the electrolysis cost-effective.[3] Among the different anodic reactions, the urea oxidation reaction (UOR, cell potential: 0.37 V) offers a more favourable pathway for supplying electrons to the coupled cathodic hydrogen evolution reaction (HER) compared to the OER (cell potential: 1.23 V).[2,4] Despite the thermodynamic advantage, the UOR is hindered by the slow reaction kinetics comprising multiple electron-transfer steps.[5]

The early studies on UOR mostly reported noble metal-based catalysts such as Ti–Pt, Ti–Pt–Ir, Ru, *etc.* with a moderate UOR activity.[6] The recent advances in 3d-transition metal-based electrocatalysts as an alternative to the highly expensive and scarce noble-metal-based materials have increased the potential of practical applications.[6–8] Among the various precious and non-precious metal-derived materials, nickel-based electrocatalysts were found to produce high UOR activity.[9,10] Under the

[a] Department of Chemistry, IIT (BHU), Varanasi, UP-221005, India. E-mail: arindam.chy@iitbhu.ac.in
[b] Institute of Nano Science and Technology, Knowledge City, Sector 81, Mohali, Punjab-140306, India

Open Access Article. Published on 16 March 2026. Downloaded on 4/27/2026 12:34:26 PM. This article is licensed under a Creative Commons Attribution-NonCommercial 3.0 Unported Licence.

Open Access Article. Published on 16 March 2026. Downloaded on 4/27/2026 12:34:26 PM. This article is licensed under a Creative Commons Attribution-NonCommercial 3.0 Unported Licence.

operating conditions, the Ni-based precatalysts undergo structural reconstruction and form nickel (oxy)hydroxide [Ni(O)OH] as the active species for the UOR.[11–13] In Ni(O)OH, the catalytically active Ni^{3+}-species facilitate the formation of a bridged conformation between the nitrogen of urea and the metal sites of the catalyst.[11,13] This bridging coordination favors urea adsorption and helps in urea oxidation.[14]

Moreover, the redox potential of Ni^{2+} to Ni^{3+} in the alkaline medium was found to be nearly identical to the electrolysis potential of urea, thereby promoting efficient UOR and resulting in an enhanced catalytic activity.[14] Therefore, the recent studies mostly focus on the formation of Ni(O)OH as the active phase with a tuned electronic and local atomic structure.[15] For example, Qiao and co-workers reported the formation of Ni(O)OH from NiS, NiSe, and NiO_x and evaluated their UOR performance.[10] The Ni(O)OH, prepared from the NiS, showed better UOR activity due to the poor adsorption of OH^- on the catalyst surface, inhibiting the OER.[10] Other reported examples of monometallic Ni-based catalysts for the UOR include Ni-BDC, Ni-BTC, and Ni-PDAA.[15]

However, the monometallic Ni-based electrocatalysts exhibit poor UOR activity due to the thermodynamic instability of the catalytically active Ni^{3+} species and high surface poisoning, resulting in a high onset potential.[16,17] Therefore, the rational design of efficient UOR electrocatalysts with optimized multi-elemental compositions and modulated electronic structures is essential.[18]

Mixed-metal (oxy)hydroxides, consisting of two or more redox active metal ions, produce distinct electronic and local geometric features, enabling synergistic control over the catalyst's electrochemical properties.[19] The doping of transition metals such as Mn, Fe, and Co in Ni(O)OH is mostly studied for the UOR.[20–22] Among these metals, Co-doped Ni(O)OH shows higher electrical conductivity compared to Mn and Fe-doping.[20] This enhanced conductivity allows Co to shift the Ni^{2+}/Ni^{3+} oxidation peak to a lower potential. For example, in the case of CoNi layered double hydroxide (CoNi-LDH), Co^{2+} is first oxidized to Co^{3+}, which then facilitates the oxidation of Ni^{2+} to Ni^{3+}.[20,21] In contrast, in NiMn-LDH, the oxidation of Ni^{2+} to Ni^{3+} takes place at a higher potential than that of Ni-LDH, resulting in a poor catalytic activity. In addition, the Mn-based redox couples ($Mn^{2+}/Mn^{3+}/Mn^{4+}$) are less effective for catalyzing the UOR due to the limited redox potential window and lower electrical conductivity.[21] Also, Mn centres interact poorly with urea molecules, limiting the ability to effectively activate and oxidize urea.[20]

Recently, our group and others have demonstrated that the precatalyst's structure and the anodic activation process have a huge impact on the electronic structure and local atomic structure of the active catalysts.[23–25] For example, PBA@NiFe/NF demonstrates an enhanced UOR and OER activity, owing to the modulation of the electronic structure, achieved through the anodic reconstruction process.[25] This reconstruction modifies the composition and electronic states of the active catalytic sites to promote faster reaction kinetics. Similarly, other structurally modified catalysts such as Mo-doped-$NiCo_2S_4$, O-NiMoP, $Co_{0.6}Ni_{0.4}$-LDH, Ni–S–Se *etc.* have shown improved UOR activity through composition tuning and structural engineering.[26–30]

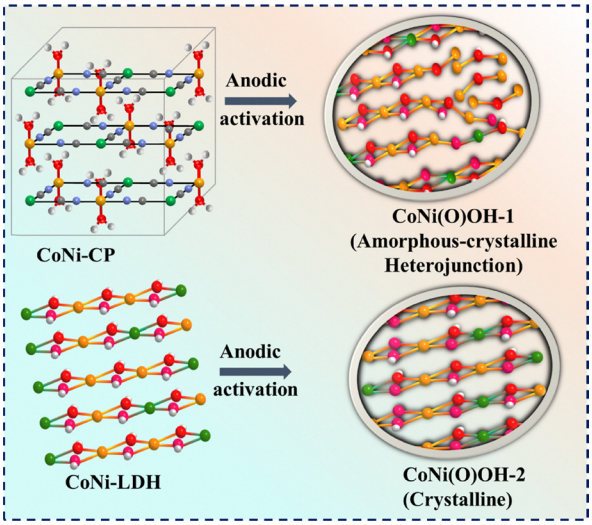

Scheme 1 Synthesis of CoNi(O)OH-1 and CoNi(O)OH-2 by the anodic activation of CoNi-CP and CoNi-LDH.

These findings motivated us to access Co–NiOOH-1 as the active catalyst by the anodic activation of a CoNi-CP (CP = coordination polymer) and explored its UOR activity (Scheme 1). The catalyst CoNi(O)OH-1 showed a far better UOR activity than that of CoNi(O)OH-2 (obtained by the anodic activation of CoNi-LDH), and Ni(O)OH (formed by the anodic activation of NiNi-CP).

The remarkable UOR activity of CoNi(O)OH-1 is attributed to the formation of the heterojunction between the amorphous and crystalline phases. The interface of the amorphous and crystalline phases improves the charge transfer property of the catalyst, redistributes the electrons, and fine-tunes the electrochemical properties.[31] Furthermore, a large number of active sites can be accessed by heterojunction formation.[32] Also, the amorphous phase with long-range disorder offers structural flexibility to stabilize the catalytic sites for the binding of the substrate and reaction intermediates.[33,34] As a result, crystalline–amorphous heterojunction electrocatalysts have been widely explored for different electrochemical energy conversion processes.[31,33]

The facile oxidation of Ni^{2+} to Ni^{3+} in CoNi(O)OH-1 improves its UOR activity compared to CoNi(O)OH-2. The CP-derived CoNi(O)OH-1 delivered an industrially relevant current density of 400 mA cm^{-2} at a remarkably low potential of 1.34 V *vs.* RHE.

Results and discussion

Syntheses and characterizations of the catalysts

The cyanide-bridged coordination polymer was synthesized by a co-precipitation method as described in the SI. In CoNi-CP, each Co^{2+} ion is coordinated to four nitrogen atoms of –CN bridges and two oxygen atoms of H_2O molecules, forming an octahedral geometry, while the Ni centers are coordinated to four carbon atoms of –CN ligands in a square-planar

© 2026 The Author(s). Published by the Royal Society of Chemistry

Open Access Article. Published on 16 March 2026. Downloaded on 4/27/2026 12:34:26 PM. This article is licensed under a Creative Commons Attribution-NonCommercial 3.0 Unported Licence.

configuration (Scheme 1). In NiNi-CP, the cationic site Co^{2+} is replaced by Ni^{2+}.

The powder X-ray diffraction (PXRD) pattern of NiNi-CP confirmed the formation of a Hofmann-type $Ni(H_2O)_2[Ni(CN)_4]\cdot xH_2O$, which is consistent with the previous literature (Fig. S1).[23,35] Similarly, CoNi-CP exhibited a PXRD pattern characteristic of a Hofmann-type structure. However, its diffraction peaks were comparatively broader and showed a negative shift of 0.17–0.20° in the 2θ value compared to those of NiNi-CP, suggesting that Co-incorporation induces lattice strain within the framework (Fig. S1). Additionally, CoNi-LDH was prepared hydrothermally by the reported procedure.[23]

The formation of the synthesized CPs was further confirmed by analyzing the –C≡N stretching vibrations by infrared (IR) spectroscopy.[36] In CoNi-CP, the –C≡N stretching vibration appeared at a higher wavenumber compared to NiNi-CP (Fig. S2).

The CPs were electrophoretically deposited on a nickel foam (NF) support (see details in the SI), and the resulting electrodes were electrochemically activated in 1.0 M KOH by cyclic voltammetry (CV) in a standard three-electrode setup.[23] The electrochemical activation of CoNi-CP, NiNi-CP, and CoNi-LDH formed CoNi(O)OH-1, Ni(O)OH, and CoNi(O)OH-2, respectively.

After electrochemical anodic activation, the catalysts were characterized to gain insight into the phase structure, morphology and electronic structure. The PXRD pattern of CoNi(O)OH-1 did not exhibit any peaks due to its poor crystallinity (Fig. S3 and more details can be found later). In contrast, Ni(O)OH displays two low-intensity peaks, indicating the formation of a semi-crystalline phase of α-$Ni(OH)_2$ (Fig. S3). In the PXRD of CoNi(O)OH-2, the sharp diffractions of α-$Ni(OH)_2$ were detected, showing its crystalline nature.[24,37]

The Raman spectra of CoNi(O)OH-1 and Ni(O)OH detected two intense signals for the E_g band and A_{1g} band, corresponding to the bending and stretching vibrations of Ni–O (Fig. 1a).[17,38] The intensity ratios of the E_g to A_{1g} peaks in CoNi(O)OH-1 and Ni(O)OH were determined to be 1.88 and 1.16, respectively, confirming a more defect-rich structure of the former (Fig. 1a). Notably, in CoNi(O)OH-1, both the E_g and A_{1g} bands appeared at higher Raman shift values (478 cm^{-1} and 568 cm^{-1}) compared to those of Ni(O)OH (472 cm^{-1} and 537 cm^{-1}), indicating a stronger Ni–O bond in the former (inset in Fig. 1a).[39]

Furthermore, X-ray photoelectron spectroscopy (XPS) analysis was performed to probe the surface electronic environments of the active catalysts (Fig. 1b).[23,40] The Ni 2p XPS of CoNi(O)OH-1, CoNi(O)OH-2, and Ni(O)OH were deconvoluted into two major peaks, Ni $2p_{3/2}$ and Ni $2p_{1/2}$.[23] The Ni $2p_{3/2}$ peak in CoNi(O)OH-1 exhibits a positive shift of 0.51 eV and 0.62 eV in the binding energy compared to CoNi(O)OH-2 and Ni(O)OH, respectively. This indicates that the Ni sites in CoNi(O)OH-1 possess a higher positive charge density compared to those in CoNi(O)OH-2 and Ni(O)OH.

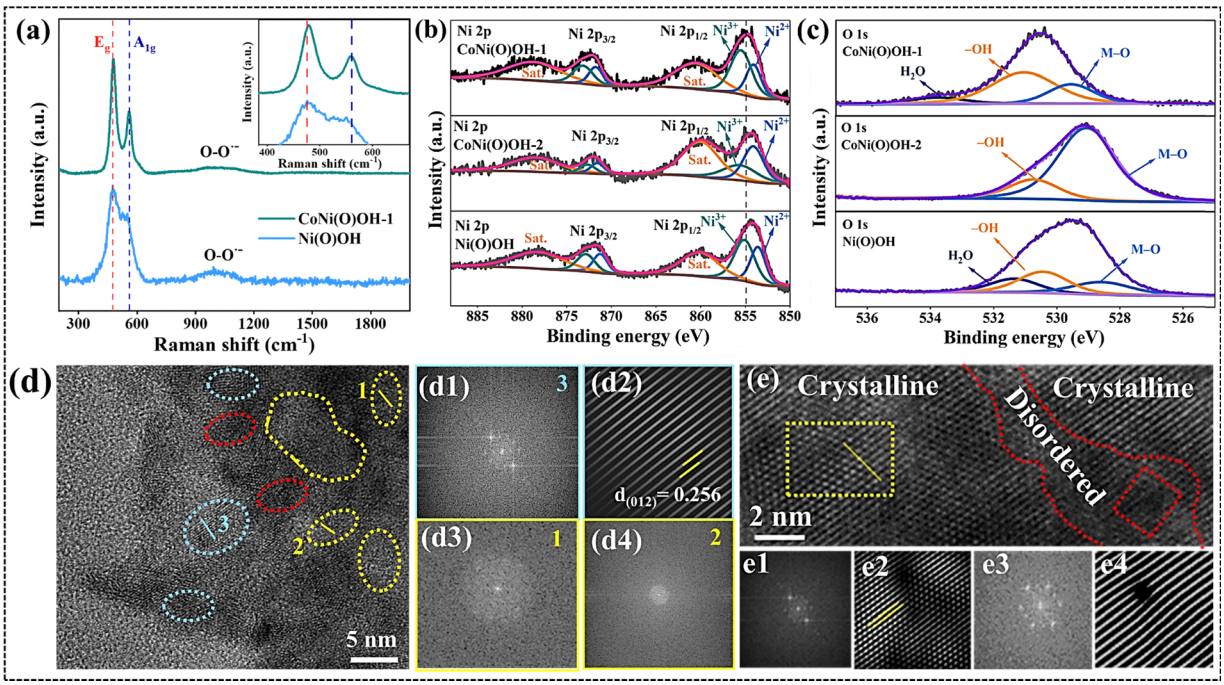

Fig. 1 (a) The Raman spectra of CoNi(O)OH-1 and Ni(O)OH show two intense bands corresponding to Ni–O bending (E_g) and Ni–O stretching (A_{1g}) vibrations along with a broad peak between 850 and 1100 cm^{-1} for superoxide species. (b) Comparison of Ni 2p XPS of CoNi(O)OH-1, CoNi(O)OH-2, and Ni(O)OH. (c) Comparison of O 1s XPS of CoNi(O)OH-1, CoNi(O)OH-2, and Ni(O)OH. (d) HRTEM image of CoNi(O)OH-1, showing the presence of crystalline (blue area) and amorphous (yellow area) phases with a defect-rich domain (red area). (d1) and (d2) The FFT and IFFT of the specified area-3 in figure (d), showing the crystalline structure with the (012) plane of Ni(O)OH. (d3) and (d4) FFT of area-1 and 2 in figure (d), showing the amorphous nature of the catalyst. (e) HRTEM image of CoNi(O)OH-1 showing the disordered domain between the crystalline phases. (e1) and (e2) The FFT and IFFT of the specified area (yellow) in figure (e), showing the (012) plane of the crystalline Ni(O)OH. (e3) and (e4) FFT and IFFT of the disordered region (red).

Open Access Article. Published on 16 March 2026. Downloaded on 4/27/2026 12:34:26 PM. This article is licensed under a Creative Commons Attribution-NonCommercial 3.0 Unported Licence.

The Ni $2p_{3/2}$ and Ni $2p_{1/2}$ peaks were further fitted into Ni^{2+} and Ni^{3+} species. The peak area ratio of Ni^{3+}/Ni^{2+} in CoNi(O)-OH-1 (2.15) was considerably higher than that of CoNi(O)OH-2 (0.9) and Ni(O)OH (1.84), implying distinct electronic structures of Ni in the three catalysts.[34,41] It should be mentioned here that the CP-derived CoNi(O)OH-1 and Ni(O)OH showed a higher amount of Ni^{3+} species than that of CoNi(O)OH-2. The higher Ni valence state in CoNi(O)OH-1 than that in CoNi(O)-OH-2 can be attributed to the facile oxidation of Ni^{2+} to Ni^{3+}. Furthermore, the Ni $2p_{3/2}$–$2p_{1/2}$ spin–orbit splitting in CoNi(O)OH-1 was found to be lower than that of the other two catalysts, indicating the presence of a higher amount of Ni^{3+} (Fig. 1b).

The Co 2p XPS signal of CoNi(O)OH-1 was found to be extremely weak due to substantial Co leaching during the anodic activation of CoNi-CP (Fig. S4).[42] In contrast, CoNi(O)OH-2 showed a well-defined Co 2p peak, with distinct Co $2p_{3/2}$ and Co $2p_{1/2}$ signals at 779.81 eV and 795.11 eV, respectively.

The O 1s spectra of the catalysts were fitted into three peaks for M–O, M–OH species, and adsorbed H_2O molecules.[43] In CoNi(O)OH-1, the M–O and M–OH peaks were observed at a higher binding energy compared to CoNi(O)OH-2 and Ni(O)OH (Fig. 1c). This result indicates the presence of a larger fraction of high-valent metal species in CoNi(O)OH-1.

The surface Co/Ni ratio in the CoNi(O)OH-1 was determined to be 0.21, indicating a significant Co leaching during the anodic activation process of CoNi-CP. In contrast, in CoNi(O)OH-2 (Co/Ni ratio: 0.74), a slight loss of Co was observed during the anodic activation of CoNi-LDH.

Furthermore, electron paramagnetic resonance (EPR) spectroscopy was employed to probe the presence of Ni^{3+} species in CoNi(O)OH-1 (Fig. S5).[44,45] The EPR spectrum showed a sharp signal at $g = 2.010$ for the paramagnetic Ni^{3+}-species ($Ni^{3+}O_6$ octahedral crystal field, low-spin $t_{2g}^6e_g^1$ electronic configuration).

The scanning electron microscopy (SEM) analyses revealed sheet-like structures for CoNi(O)OH-1 and Ni(O)OH (Fig. S6 and S7). The energy dispersive X-ray (EDX) spectroscopy of CoNi(O)OH-1 revealed the presence of Co, Ni, and O (Fig. S8). The transmission electron microscopy (TEM) of CoNi(O)OH-1 showed a nanosheet morphology (Fig. 1d, S9a–d).

In contrast to the PXRD results, the high-resolution TEM (HRTEM) detected the lattices of Ni(O)OH along with the amorphous region in the nanosheets of CoNi(O)OH-1 (Fig. 1d and e).[24,46] In addition, a highly defect-rich structure with lattice distortion and dislocation between the crystalline and amorphous region was also observed (Fig. 1d and e).[31,47] The crystalline domain (light blue circles) showed clear lattice fringes with a *d*-spacing of 0.256 nm, corresponding to the (012) plane of Ni(O)OH (Fig. 1d1, d2, S9).[29,48,49] The fast Fourier transform (FFT) analyses at different amorphous regions (yellow dotted circle, regions 1 and 2) detected blurred rings (no diffraction points), showing the amorphous nature (Fig. 1d and d3, d4, S9).[47] A highly disordered structure was observed between the two crystalline domains. This was further confirmed by the corresponding FFT and inverse FFT analyses (Fig. 1e, S9).

The coexistence of amorphous and crystalline phases makes CoNi(O)OH-1 unique and improves its charge-transfer capability, thereby optimizing its overall electrochemical performance. This mixed-phase nature with a highly disordered structure could not be distinctly detected in the PXRD pattern due to inherent diffraction limitations.

Electrochemical performance

Cyclic voltammetry (CV) was carried out to understand the redox behavior of the catalysts in the alkaline medium. CV profiles showed the facile oxidation of Ni^{2+} to Ni^{3+} in CoNi(O)OH-1 (1.35 V *vs.* RHE) compared to Ni(O)OH (1.41 V *vs.* RHE). This result shows that the incorporation of Co in Ni(O)OH lowers the anodic potential required for Ni^{2+} oxidation (Fig. S10).

The OER performance of the catalysts was assessed through linear sweep voltammetry (LSV) studies. CoNi(O)OH-1 delivered 200 mA cm^{-2} current density at an overpotential of 290 mV, while Ni(O)OH and CoNi(O)OH-2 required 505 mV and 460 mV overpotentials, respectively (Fig. 2a). These results confirm the superior OER performance of the electrochemically produced CoNi(O)OH-1.

The Tafel slopes of the active catalysts were calculated to be 45 mV dec^{-1}, 120 mV dec^{-1}, and 167 mV dec^{-1} for CoNi(O)OH-1, CoNi(O)OH-2, and Ni(O)OH, respectively, revealing faster OER kinetics with CoNi(O)OH-1 (Fig. S11).[43] Interestingly, the Tafel slope of CoNi(O)OH-1 was less than 59 mV dec^{-1} and very close to 40 mV dec^{-1}, indicating an intrinsic high electrochemical activity. Additionally, the low Tafel slope value suggests the formation of surface-adsorbed –OOH species as the rate-determining step (detected by Raman spectroscopy also, see later).

Furthermore, electrochemical impedance spectroscopy (EIS) demonstrated the lowest charge-transfer resistance for CoNi(O)OH-1 among the synthesized catalysts (Fig. S12).

The electrochemical surface area (ECSA) was determined from the double-layer capacitance (C_{dl}), conducting CV in the non-faradaic region at varying scan rates.[43] CoNi(O)OH-1 showed the highest C_{dl} value (7.1 mF cm^{-2}) among the synthesised catalysts (Fig. S13). The ECSA-normalised current density was employed to evaluate the specific activity (SA) of the catalysts to follow the order: CoNi(O)OH-1 > CoNi(O)OH-2 > Ni(O)OH (Fig. S14).

Consistently, CoNi(O)OH-1 possessed the highest number of electrochemically active sites among the catalysts considered in this study (Fig. S15).

Electrochemical urea oxidation

Furthermore, the urea oxidation activity of all the anodically activated catalysts was evaluated. Among all the synthesized catalysts, CoNi(O)OH-1 exhibited the best UOR activity (Fig. 2b). CoNi(O)OH-1 achieved the industrial-level benchmark current density of 400 mA cm^{-2} at 1.34 V *vs.* RHE, while CoNi(O)OH-2 and Ni(O)OH reached the same current density at a much higher applied potential (Fig. 2c and d). Notably, the applied potential for the UOR achieved by CoNi(O)OH-1 surpasses that of most of the reported cobalt–nickel-based catalysts (Table S1).[27]

© 2026 The Author(s). Published by the Royal Society of Chemistry

Open Access Article. Published on 16 March 2026. Downloaded on 4/27/2026 12:34:26 PM.
This article is licensed under a Creative Commons Attribution-NonCommercial 3.0 Unported Licence.

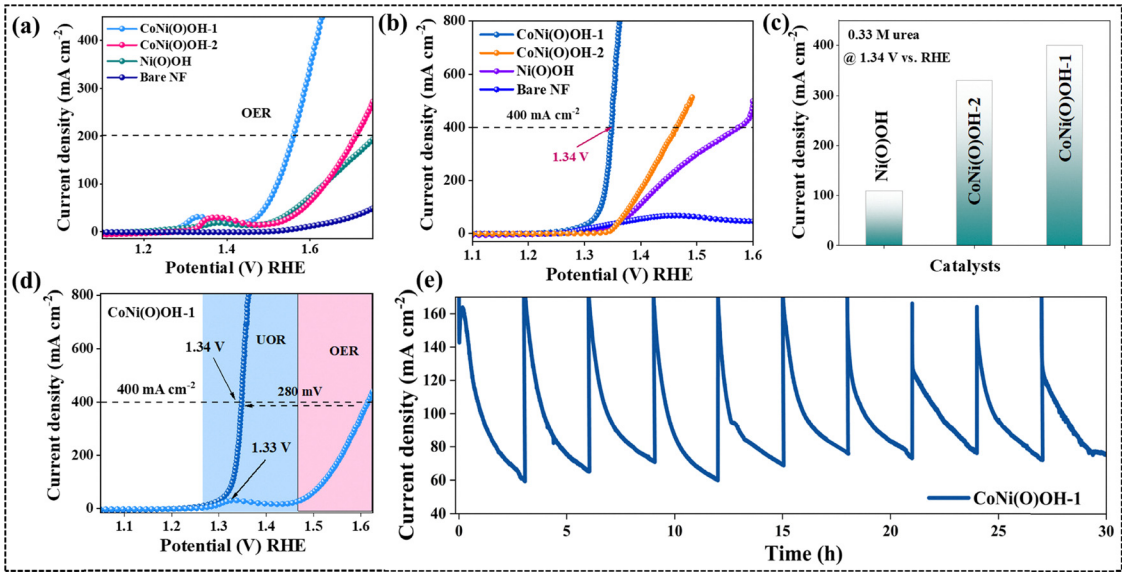

Fig. 2 (a) The LSV profiles of CoNi(O)OH-1, CoNi(O)OH-2, and Ni(O)OH during the OER. (b) The LSV profiles of CoNi(O)OH-1, CoNi(O)OH-2, Ni(O)OH, and bare NF during the UOR (reaction conditions: 1.0 M KOH + 0.33 M urea at a scan rate of 5 mV s^{-1}). (c) Comparison of the current densities of CoNi(O)OH-1, CoNi(O)OH-2, and Ni(O)OH at a constant potential for urea oxidation. (d) The LSV curves of CoNi(O)OH-1 for the OER and UOR, showing a significant improvement in the potential requirement for the UOR. (e) The chronoamperometric (CA) profile of CoNi(O)OH-1 over 10 consecutive UOR cycles.

Cyanide-bridged coordination polymer CoNi-CP undergoes anodic reconstruction, during which Co sites facilitate the oxidation of Ni^{2+} to Ni^{3+} and partially leach out from the catalyst structure.[23,50,51] This Co-assisted oxidation of Ni^{2+} and simultaneous Co leaching are the key features of the activation process that produce the highly active Co-doped-Ni(O)OH as the active phase. In addition, the electronic structure modulation and the formation of the crystalline–amorphous heterojunction in CoNi(O)OH-1 offer an improved electrochemical performance compared to CoNi(O)OH-2.[49] The facile Ni^{2+} to Ni^{3+} transition also accelerates the reaction kinetics in CoNi(O)OH-1. The synergistic effect of the above factors led to a pronounced improvement in both the OER and urea oxidation activities of CoNi(O)OH-1 compared to those of Ni(O)OH and CoNi(O)OH-2.

Additionally, the UOR activity of CoNi(O)OH-1 was evaluated under varying urea concentrations. At a 0.33 M concentration of urea, CoNi(O)OH-1 exhibited the highest activity (Fig. S16). However, when the urea concentration was reduced to 0.1 M or increased to 0.5 M, the current density was significantly decreased. The decrease in UOR in 0.1 M urea solution can be explained by the low availability of the substrate, while the poor current density at a higher urea concentration can be ascribed to the unavailability of the active sites due to the coverage by the excess substrate (Fig. S16).

Furthermore, the stability of CoNi(O)OH-1 in the UOR was evaluated under chronoamperometry (CA) conditions (Fig. 2e). CoNi(O)OH-1 underwent the UOR for 10 consecutive cycles, showing stability for 30 h.

Mechanism of urea oxidation

To understand the UOR activity of CoNi(O)OH-1, *operando* Raman spectroscopy was carried out in the potential range 1.20 V *vs.* RHE to 1.60 V *vs.* RHE with and without the addition of urea to the electrolyte (1.0 M KOH solution). The *operando* study revealed different behaviours of the catalyst under UOR and OER conditions (Fig. 3a and S17).[10,52]

Upon applying a potential, CoNi(O)OH-1 showed characteristic peaks at 472 cm^{-1} and 540 cm^{-1} corresponding to the E_g bending and A_{1g} stretching modes, respectively, of the Ni–O bond.[53–55] When the potential was raised from 1.20 V to 1.60 V *vs.* RHE, the intensity of the peaks corresponding to the Ni–O bond was increased. This shows that as the potential increases, more (oxy)hydroxide sites are formed.[55]

When 0.33 M urea was added to the KOH solution, the Raman spectra showed an additional peak at 1005 cm^{-1} corresponding to the C–N stretching of the urea molecule. The intensity of the E_g and A_{1g} bands was found to be weak in the potential range of 1.20 to 1.50 V *vs.* RHE (Fig. 3a). A further increase in the applied anodic potential (1.60 V *vs.* RHE) led to an increase in the intensity of the E_g and A_{1g} bands due to the suppression of the UOR and the dominance of the OER. It is also observed that after 1.5 V, the E_g band intensity increases, indicating a gradual structural change and the formation of high valent Ni–O species. Interestingly, the peak intensity of the C–N bond was also increased up to 1.5 V *vs.* RHE, and at higher potential (1.6 V *vs.* RHE), the peak intensity was decreased.

Therefore, the *operando* Raman study reveals potential-dependent UOR and OER activity on the CoNi(O)OH-1 surface. In the potential range of 1.20–1.50 V *vs.* RHE, the UOR prevails over the OER, whereas the reverse situation is observed when the potential exceeds 1.60 V *vs.* RHE. This is consistent with the results reported in the literature for urea oxidation over nickel-based catalysts.[6,10,55]

Based on the Raman study, the UOR on CoNi(O)OH-1 proceeds through: (i) the electrochemical-chemical pathway involving urea

Open Access Article. Published on 16 March 2026. Downloaded on 4/27/2026 12:34:26 PM.
This article is licensed under a Creative Commons Attribution-NonCommercial 3.0 Unported Licence.

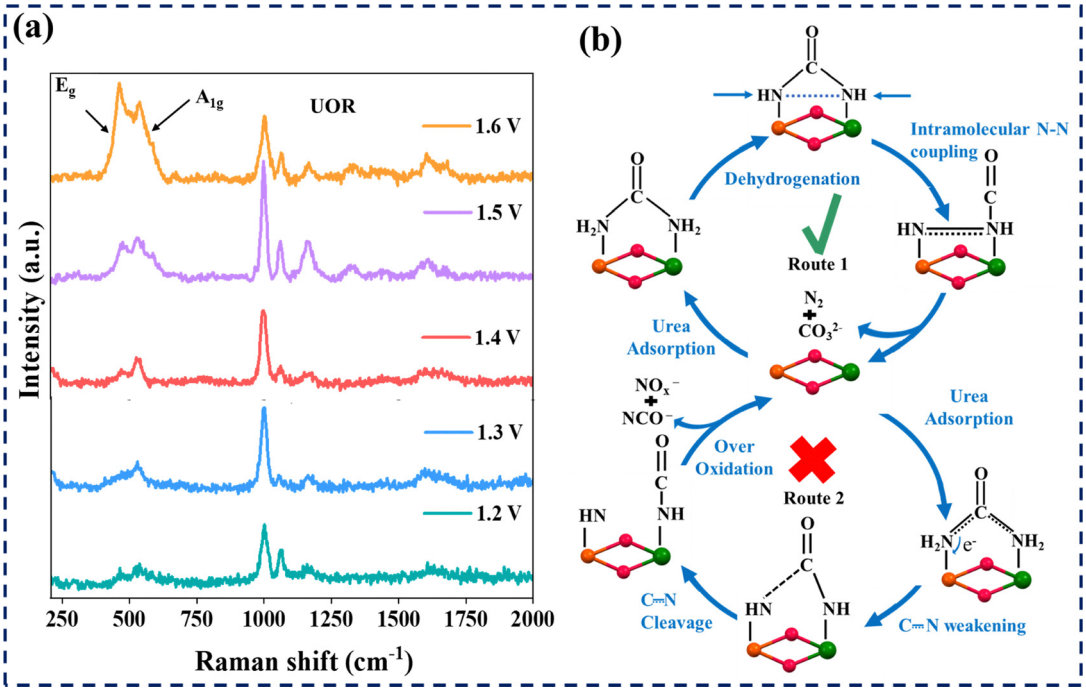

Fig. 3 (a) *Operando* Raman spectroscopy at varied potentials during the UOR with CoNi(O)OH-1 in 1.0 M KOH and 0.5 M urea; (b) proposed UOR mechanism on CoNi(O)OH-1 by intra-molecular N–N coupling.

adsorption on CoNi(O)OH-1 followed by electron transfer, and (ii) catalyst regeneration *via* dehydrogenation (Fig. 3b).[10]

In the electrochemical–chemical route, Ni^{2+} is first oxidized to high-valent Ni^{3+}–O species, which subsequently react with the adsorbed urea, following the sequential dehydrogenation and N–N coupling to form CO_3^{2-}, N_2, and H_2O (Fig. 3b). Raman spectroscopy also detected the adsorbed CO_3^{2-} (1065 cm^{-1}) (Fig. 3).[27] After the completion of the UOR, the catalyst CoNi(O)OH-1 was regenerated. Interestingly, neither NCO^- nor NO_x^- was detected on the CoNi(O)OH-1 surface, indicating that the C–N bond was well stabilized prior to intramolecular N–N coupling (Fig. 3).[56]

The UOR on CoNi(O)OH-1 was further evaluated in a two-electrode water electrolyzer by using it as both the anode and cathode. CoNi(O)OH-1 achieved a current density of 100 mA cm^{-2} for overall water splitting (HER‖OER) at a cell voltage of 1.95 V (Fig. S18 and S19). Remarkably, upon introducing urea into the electrolyte, the required cell voltage for HER‖UOR at the same current density decreased to 1.66 V, representing a 301 mV gain in potential compared to HER‖OER. Additionally, CoNi(O)OH-1 also demonstrated a significantly lower cell voltage requirement than CoNi(O)OH-2 (Fig. S18 and S19).

Post-catalytic characterizations

After the UOR, CoNi(O)OH-1 was characterized to examine phase and structural changes. The PXRD pattern of CoNi(O)OH-1 after the UOR showed no noticeable changes (Fig. S20).

The XP spectra detected a significant difference in the surface electronic structure of CoNi(O)OH-1 after the UOR. The Ni $2p_{3/2}$ peak was shifted towards a lower binding energy after the UOR (Fig. S21). Furthermore, an increase in the Ni $2p_{3/2}$–$2p_{1/2}$ spin–orbit coupling was observed in the UOR catalyst (17.71 eV) compared to that in the CoNi(O)OH-1 (17.34 eV). A decrease in the Ni^{3+}/Ni^{2+} ratio (0.54) after the UOR was also observed compared to the OER catalyst (Ni^{3+}/Ni^{2+} = 1.2).

Furthermore, the Co 2p XPS of CoNi(O)OH-1 showed poor signals due to the low amount of Co in the catalyst (Fig. S22). The O 1s spectra of CoNi(O)OH-1 were fitted into two peaks corresponding to M–O and –OH groups (Fig. S22).

The HR-TEM of CoNi(O)OH-1 after the UOR showed similar features to the fresh catalyst. All three regions, crystalline, amorphous and disordered, were clearly visible (Fig. S23).

Conclusions

In summary, CoNi(O)OH-1, produced by the electrochemical activation of CoNi-CP, showed outstanding electrocatalytic urea oxidation due to the formation of a crystalline–amorphous heterojunction with structural disorder. Furthermore, the Co species enhances the catalyst's electrical conductivity, enabling efficient charge transport during the electrochemical process. This facilitates the oxidation of Ni^{2+} to the catalytically active Ni^{3+} sites. The XPS and EPR spectra confirm the presence of the paramagnetic low-spin Ni^{3+} species in CoNi(O)OH-1. *Operando* Raman spectroscopy reveals that the UOR with CoNi(O)OH-1 proceeds through successive dehydrogenation steps, followed by C–N bond cleavage.

Author contributions

T. Ansari was involved in the syntheses, characterization, and data analysis. V. Patel was involved in the Raman characterization.

© 2026 The Author(s). Published by the Royal Society of Chemistry

Open Access Article. Published on 16 March 2026. Downloaded on 4/27/2026 12:34:26 PM. This article is licensed under a Creative Commons Attribution-NonCommercial 3.0 Unported Licence.

M. Dhillan and A. Basu were involved in the microscopic characterization of the catalyst. The planning, design, and supervision of the research, as well as the manuscript editing, were carried out by A. Indra. The final version of the manuscript has been reviewed and approved by all authors.

Conflicts of interest

There are no conflicts to declare.

Data availability

The data supporting this article have been included as part of the supplementary information (SI). Supplementary information: synthesis and characterization of the catalysts, electrochemical data, and characterization of the products. See DOI: https://doi.org/10.1039/d5ey00367a.

Acknowledgements

The financial support from the ANRF (grant no. CRG/2023/002395), Government of India, is gratefully acknowledged. T. Ansari acknowledges the PMRF (PMRF ID: 1103080), while V. Patel is thankful to the IIT (BHU) for financial support.

References

1 T. E. Jones, D. Teschner and S. Piccinin, *Chem. Rev.*, 2024, **124**, 9136–9223.
2 X. Wang, J. P. Li, Y. Duan, J. Li, H. Wang, X. Yang and M. Gong, *ChemCatChem*, 2022, **14**, 202101906.
3 B. Dasgupta, D. Bagchi, T. Sontheimer, M. Driess and P. W. Menezes, *Nat. Rev. Chem.*, 2025, **9**, 766–789.
4 W. Ge, L. Lin, S. Q. Wang, Y. Wang, X. Ma, Q. An and L. Zhao, *J. Mater. Chem. A*, 2023, **11**, 15100–15121.
5 X. Gao, S. Zhang, P. Wang, M. Jaroniec, Y. Zheng and S. Z. Qiao, *Chem. Soc. Rev.*, 2024, **53**, 1552–1591.
6 G. Zhan, L. Hu, H. Li, J. Dai, L. Zhao, Q. Zheng, X. Zou, Y. Shi, J. Wang, W. Hou, Y. Yao and L. Zhang, *Nat. Commun.*, 2024, **15**, 5918.
7 T. Li, Z. Zheng, Z. Chen, M. Zhang, Z. Liu, H. Chen, X. Xiao, S. Wang, H. Qu, Q. Fu, L. Liu, M. Zhou, B. Wang and G. Zhou, *Energy Environ. Sci.*, 2025, **18**, 4996–5008.
8 Nitika and R. K. Dutta, *Adv. Sustainable Syst.*, 2025, **09**, e00700.
9 S. M. Peng, S. T. Chang, C. C. Chang, P. Han, C. C. Chang, K. C. Wu, Y. H. Huang, Y. C. Chen, T. R. Kuo, C. W. Pao, J. L. Chen and D. Y. Wang, *J. Mater. Chem. A*, 2024, **12**, 24126–24135.
10 X. Gao, X. Bai, P. Wang, Y. Jiao, K. Davey, Y. Zheng and S. Z. Qiao, *Nat. Commun.*, 2023, **14**, 5842.
11 X. Gao, J. Dong, H. Yang, C. Ni, X. He, Z. Li and L. Tian, *J. Alloys Compd.*, 2025, **1012**, 178477.
12 N. N. Rao, C. Alex, M. Mukherjee, S. Roy, A. Tayal, A. Datta and N. S. John, *ACS Catal.*, 2024, **14**, 981–993.
13 J. Li, S. Wang, J. Chang and L. Feng, *Adv. Powder Mater.*, 2022, **1**, 100030.
14 Z. Li, Y. Zheng, H. Guo, X. Cheng, Y. Huang, C. Liu and J. Zang, *J. Alloys Compd.*, 2024, **1008**, 176591.
15 X. Zhang, S. Feizpoor, M. Humayun and C. Wang, *Chem Catal.*, 2024, **04**, 100840.
16 S. Xu, X. Ruan, M. Ganesan, J. Wu, S. K. Ravi and X. Cui, *Adv. Funct. Mater.*, 2024, **34**, 2313309.
17 M. Liu, W. Zou, J. Cong, N. Su, S. Qiu and L. Hou, *Small*, 2023, **19**, 2302698.
18 H. Sun and S. Song, *Small*, 2024, **20**, 2401343.
19 Z. Zheng, D. Wu, L. Chen, S. Chen, H. Wan, G. Chen, N. Zhang, X. Liu and R. Ma, *Appl. Catal., B*, 2023, **340**, 123214.
20 X. Yang, H. Zhang, W. Xu, B. Yu, Y. Liu and Z. Wu, *Catal. Sci. Technol.*, 2022, **12**, 4471–4485.
21 S. Rajalekshmi, K. Sooriya, S. Varsha and A. Pandikumar, *Catal. Sci. Technol.*, 2025, **15**, 5753–5764.
22 Z. Ji, Y. Song, S. Zhao, Y. Li, J. Liu and W. Hu, *ACS Catal.*, 2022, **12**, 569–579.
23 T. Ansari, D. Bagchi, S. Ghosh, J. Niklas Hausmann, A. Indra and P. W. Menezes, *Chem. – Eur. J.*, 2025, **31**, 202404174.
24 A. Yadav, T. Ansari, P. Mannu, B. Singh, A. K. Singh, Y. C. Huang, V. Kumar, S. Singh, C. L. Dong and A. Indra, *J. Mater. Chem. A*, 2024, **12**, 29072–29080.
25 X. Liu, J. Zhang, L. Jin, C. Chen, J. He, Q. Xu and J. Lu, *Inorg. Chem.*, 2023, **62**, 3637–3645.
26 N. Nwaji, B. Fikadu, M. Osial, M. Warczak, Z. Moazzami Goudarzi, M. Gniadek, S. Asgaran, J. Lee and M. Giersig, *Small*, 2025, **21**, 2410848.
27 H. Jiang, M. Sun, S. Wu, B. Huang, C.-S. Lee and W. Zhang, *Adv. Funct. Mater.*, 2021, **31**, 2104951.
28 Y. Jeon, J. Medvedev, Y. Seong, X. Medvedeva, C. Bae, J. Kim, A. Klinkova and J. Kim, *EcoMat*, 2024, **7**, e12510.
29 N. Chen, Y.-X. Du, G. Zhang, W.-T. Lu and F.-F. Cao, *Nano Energy*, 2021, **81**, 105605.
30 J. Zhang, J. Feng, J. Zhu, L. Kang, L. Liu, F. Guo, J. Li, K. Li, J. Chen, W. Zong, M. Liu, R. Chen, I. P. Parkin, L. Mai and G. He, *Angew. Chem., Int. Ed.*, 2024, **63**, 202407038.
31 X. Wang, Z. Zhang, H. Zhang, S. Lin, C. Li, Y. Xie, Y. Zhang, S. Feng, D. Liu and Z. Wang, *Adv. Funct. Mater.*, 2025, **35**, 14137.
32 L. Jin, R. Ji, H. Wan, J. He, P. Gu, H. Lin, Q. Xu and J. Lu, *ACS Catal.*, 2023, **13**, 837–847.
33 L. Yao, X. Wu, Z. Geng, Y. Zhang, Y. Fang, Q. Zhu, N. Liang, M. Cai, H. Sai, J. Cheng, S. Li, Y. Wang, M. Han, K. Huang and S. Feng, *ACS Nano*, 2025, **19**, 5851–5859.
34 W. Cai, R. Chen, H. Yang, H. B. Tao, H. Y. Wang, J. Gao, W. Liu, S. Liu, S. F. Hung and B. Liu, *Nano Lett.*, 2020, **20**, 4278–4285.
35 X. Y. Yu, Y. Feng, B. Guan, X. W. D. Lou and U. Paik, *Energy Environ. Sci.*, 2016, **9**, 1246–1250.
36 B. Singh, P. Mannu, Y. C. Huang, R. Prakash, S. Shen, C. L. Dong and A. Indra, *Angew. Chem., Int. Ed.*, 2022, **61**, e202211585.

Open Access Article. Published on 16 March 2026. Downloaded on 4/27/2026 12:34:26 PM.
This article is licensed under a Creative Commons Attribution-NonCommercial 3.0 Unported Licence.

37 T. H. Wu and B. W. Hou, *Catal. Sci. Technol.*, 2021, **11**, 4294–4300.
38 M. Qiu, X. Zhu, S. Bo, K. Cheng, N. He, K. Gu, D. Song, C. Chen, X. Wei, D. Wang, Y. Liu, S. Li, X. Tu, Y. Li, Q. Liu, C. Li and S. Wang, *CCS Chem.*, 2023, **5**, 2617–2627.
39 A. Yadav, T. Ansari, V. Kumar and A. Indra, *ACS Appl. Nano Mater.*, 2025, **8**, 23731–23739.
40 X. Zhou, J. Hu, S. Ajmal, D. Xiang, Z. Sun, W. Chen, M. Zhu, P. Chen and P. Li, *Chem. Commun.*, 2023, **59**, 12152–12155.
41 B. Singh, R. Kumar, T. Ansari, A. Indra and A. Draksharapu, *Chem. Commun.*, 2024, **60**, 9432–9435.
42 B. Singh, T. Ansari, N. Verma, Y. C. Huang, P. Mannu, C. L. Dong and A. Indra, *J. Mater. Chem. A*, 2024, **12**, 19321–19330.
43 P. Maurya, T. Ansari and A. Indra, *Chem. Commun.*, 2023, **59**, 13359–13362.
44 J. Zhang, H. Wang, Y. Tian, Y. Yan, Q. Xue, T. Chen, Y. Zhao and X. Sun, *Adv. Funct. Mater.*, 2017, **27**, 1703483.
45 T. Hu, F. Wang, Q. Wang, L. Zhang and Y. Wang, *ACS Appl. Nano Mater.*, 2025, **8**, 771–779.
46 S. Parvin, E. Aransiola, M. Ammar, S. Lee, L. Zhang, J. Weber and J. Baltrusaitis, *ACS Appl. Mater. Interfaces*, 2024, **16**, 67715–67729.
47 Z. Gong, M. Xu, P. Li, G. Ye, W. Li and H. Fei, *ACS Catal.*, 2025, **15**, 20958–20967.
48 X. Gao, W. Feng, Z. Zhu, Z. Wu, S. Li, S. Kan, X. Qiu, A. Guo, W. Chen and K. Yin, *Adv. Mater. Interfaces*, 2021, **8**, 2002133.
49 J. L. Gunjakar, A. I. Inamdar, B. Hou, S. Cha, S. M. Pawar, A. A. Abu Talha, H. S. Chavan, J. Kim, S. Cho, S. Lee, Y. Jo, H. Kim and H. Im, *Nanoscale*, 2018, **10**, 8953–8961.
50 B. Singh, T. Ansari and A. Indra, *J. Mater. Chem. A*, 2025, **13**, 24925–24932.
51 P. Jain and P. P. Ingole, *Chem. Phys. Impact*, 2024, **9**, 100693.
52 J. Gautam, S. Y. Lee and S. J. Park, *Adv. Energy Mater.*, 2025, **15**, 2406047.
53 D. Li, X. Zhou, Q. Ruan, L. Liu, J. Liu, B. Wang, Y. Wang, X. Zhang, R. Chen, H. Ni, C. Huang, H. Wang and P. K. Chu, *Adv. Funct. Mater.*, 2024, **34**, 2313680.
54 M. Liu, W. Zou, S. Qiu, N. Su, J. Cong and L. Hou, *Adv. Funct. Mater.*, 2024, **34**, 2310155.
55 J. Zhang, J. Zhu, L. Kang, Q. Zhang, L. Liu, F. Guo, K. Li, J. Feng, L. Xia, L. Lv, W. Zong, P. R. Shearing, D. J. L. Brett, I. P. Parkin, X. Song, L. Mai and G. He, *Energy Environ. Sci.*, 2023, **16**, 6015–6025.
56 J. Dabboussi, R. A. Eichel, H. Kungl, R. Abdallah and G. Loget, *Curr. Opin. Electrochem.*, 2024, **45**, 101468.

© 2026 The Author(s). Published by the Royal Society of Chemistry